Journal Pre-proof

Imaging the Kirkendall effect in pyrite (FeS$_2$) thin films:
cross-sectional microstructure and chemical features

Carlos Morales , Dietmar Leinen , Eduardo Flores ,
Esmeralda Muñoz-Cortes , Fabrice Leardini , Jose R. Ares ,
Jan Ingo Flege , Leonardo Soriano , Isabel J. Ferrer ,
Carlos Sanchez

Please cite this article as: Carlos Morales , Dietmar Leinen , Eduardo Flores ,
Esmeralda Muñoz-Cortes , Fabrice Leardini , Jose R. Ares , Jan Ingo Flege , Leonardo Soriano ,
Isabel J. Ferrer , Carlos Sanchez , Imaging the Kirkendall effect in pyrite (FeS$_2$) thin
films: cross-sectional microstructure and chemical features, *Acta Materialia* (2020), doi:
https://doi.org/10.1016/j.actamat.2020.116582

Imaging the Kirkendall effect in pyrite (FeS$_2$) thin films: cross-sectional microstructure and chemical features

Carlos Morales[1,2], Dietmar Leinen[3], Eduardo Flores[4], Esmeralda Muñoz-Cortes[5], Fabrice Leardini[5,6], Jose R. Ares[5], Jan Ingo Flege[2], Leonardo Soriano[1,6], Isabel J. Ferrer[5,6] and Carlos Sanchez[5,6].*

[1] *Dpto. de Física Aplicada, Facultad de Ciencias, Universidad Autónoma de Madrid, Francisco Tomás y Valiente 7, E-28049 Madrid, Spain.*

[2] *Applied Physics and Semiconductor Spectroscopy, Brandenburg University of Technology Cottbus–Senftenberg, Konrad-Zuse-Strasse 1, D-03046 Cottbus, Germany*

[3] *Departamento de Física Aplicada I, Facultad de Ciencias, Universidad de Málaga, Campus Teatinos, Málaga, C.P. 29071, Spain*

[4] *FINDER-group, Instituto de Micro y Nanotecnología, IMN-CNM, CSIC (CEI UAM+CSIC) Isaac Newton, 8, E-28760, Tres Cantos, Madrid, Spain*

[5] *Dpto. de Física de Materiales, Facultad de Ciencias, Universidad Autónoma de Madrid, Francisco Tomás y Valiente 7, E-28049 Madrid, Spain.*

[6] *Instituto Nicolás Cabrera, Universidad Autónoma de Madrid, Francisco Tomás y Valiente 7, E-28049 Madrid, Spain*

[*]*Corresponding author: email: eduardo.flores@csic.es*

Graphical abstracts
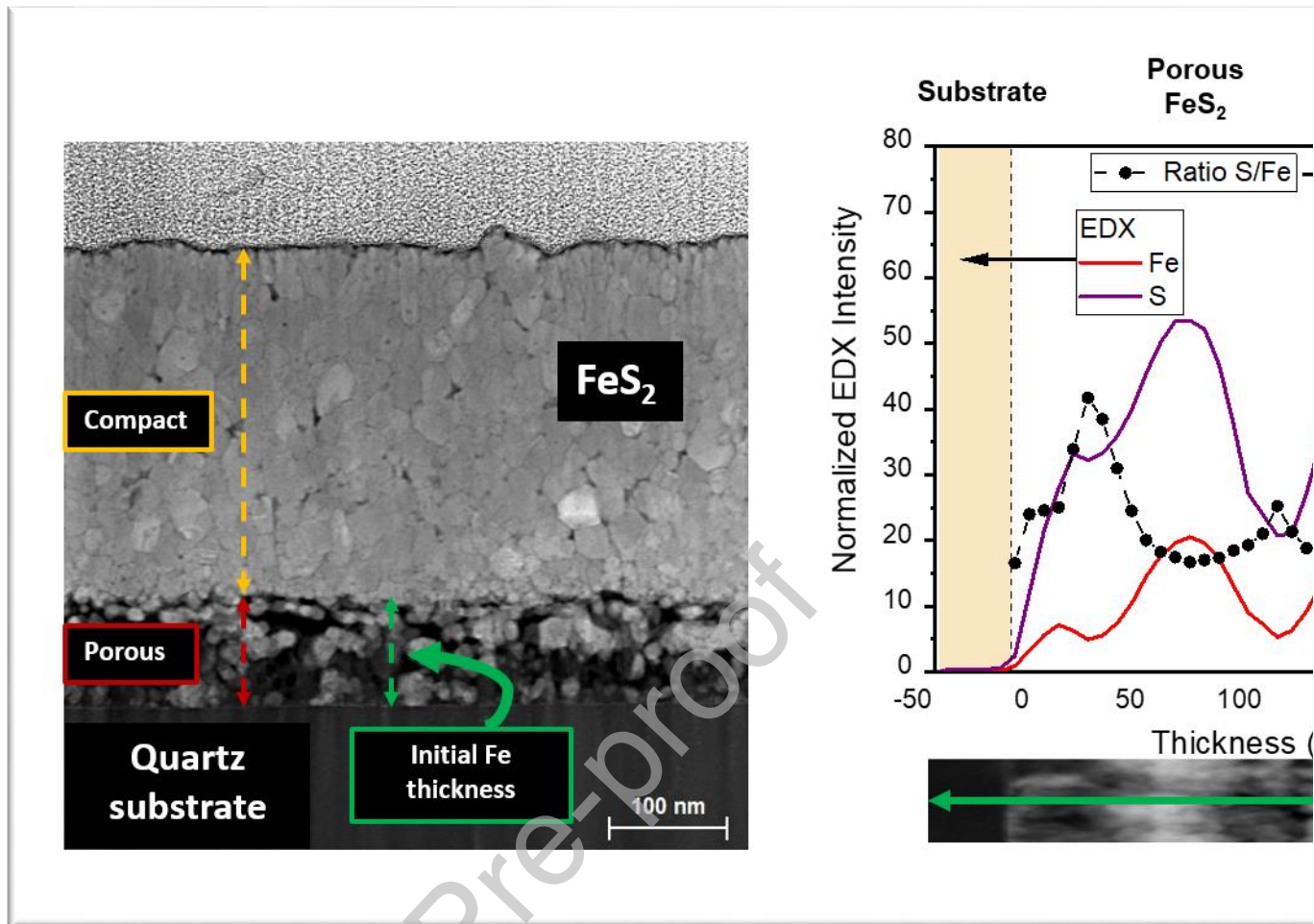
Abstract

This investigation provides novel data on the structure and chemical composition of pyrite thin films and new hints concerning their formation mechanism. From TEM-HAADF data, it has been found that the films are composed of two different layers: one is very compact and the other one is quite porous with many voids separating a few groups of grains. This porous layer is always in direct contact with the substrate, and its thickness is quite similar to that of the original Fe film. The average size of pyrite grains is equal in both layers, what suggests that the same process is responsible for their formation. Concentration profiles of sulfur, iron and some impurities (mainly sodium and oxygen from the glass substrate) through both layers are given in this work, and thus chemical inhomogeneities of the films are proved by the obtained stoichiometric ratios ($S/_{Fe}$). Moreover, Na from sodalime glass substrates mainly accumulates at the pyrite grain boundaries and barely dopes them. The obtained results support the hypothesis that the iron sulfuration process essentially induces the diffusion of iron atoms, what leads to the porous layer formation as a manifestation of the Kirkendall Effect. Therefore, it seems that the same mechanisms that operate in the synthesis of surface hollow structures at the nanoscale are also active in the formation of pyrite thin films ranging from several tens to hundreds of nanometers.

Keywords: Pyrite, TEM, cross-section, Kirkendall effect, sodium doping.

1. Introduction

The increasing demand of energy together with the environmental problems derived from the consumption of conventional energy supplies have promoted the

exploitation of new energy sources (mainly renewable and clean). The most promising of these sources is the solar one, which may be directly converted into electric energy by solar cells made from photovoltaic materials in different configurations [1] . In this context, pyrite (FeS_2) has recently recovered the researchers' attention [1−5] due to the abundance of its elements, its environmental goodness and the possibility to synthesize pyrite thin films, single crystals and nanostructures [6−9]. In addition, pyrite is considered a very promising material for solar energy conversion processes due to its very convenient bandgap (0.9-1.0 eV [10,11]) and high optical absorption coefficient ($\alpha \sim 10^5$ cm^{-1}) in a significant part of the solar radiation spectrum, what would allow to design very thin photovoltaic devices. Moreover, both n- and p-type pyrite films can be synthetized by using different dopants [12−15] which enables the fabrication of both homo and heterostructures based devices. However, photovoltaic pyrite applications are presently limited mainly due to the reduced open circuit photovoltage obtained under solar irradiation ($V_{OC} \sim 0.3$ V). The existence of an inversion layer at the pyrite surface, the presence of a high density of deep donor states within the pyrite bulk, etc., are subjects presently investigated as possible causes of that limitation [16−18]. Besides, bulk characterization has been also the focus of some works looking to explain the general p-type behavior of synthetic pyrite films in contrast with the n-type nature of synthetic single crystals [15,19−21]. Similarly, the study of the role of defects located at both surface and bulk (such as iron and sulfur vacancies) or the presence of secondary crystalline and/or amorphous phases (such as FeS_x) at the pyrite grain boundaries [18,22−24] continue to be some of the subjects that still remain open.

In this regard, it must be considered that the macroscopic properties of an artificially synthesized material strongly depend on the selected growth technique and its corresponding experimental parameters. Thus, different temperatures, reaction times,

initial precursors, etc., will determine some of the characteristics (stoichiometric relationships, purity of the pretended phase, type and density of particular defects or crystallization features) of the synthesized material. According to the existing literature, pyrite thin films show an appreciable variety of properties depending on the method used to grow them: sulfuration of iron thin films [3–5,14,15,25], chemical vapor deposition [26–29], sputtering [30,31], flash evaporation [11], spray pyrolysis [32], molecular ink-based techniques [33], hydrothermal processes [2], or electrodeposition [34]. In spite of the easiness to synthesize pyrite thin films, the details of their formation mechanism are not yet fully explained. Therefore, contributions to better know the formation mechanism of pyrite films are essential in order to reach an improved understanding and control of their characteristics.

Due to its simplicity, one of the methods most frequently used to obtain pyrite thin films is the so-called sulfuration of iron thin films [35]. Although different routes can be followed to that aim depending on the sulfur chemical form or the oxidation extent of the iron film, very frequently sulfur vapor from elemental sulfur is used to produce the sulfuration of as deposited iron thin films. One of the advantages of this method is that several experimental parameters, which can be isolated from one another, play a significant role in determining the characteristics of the resulting pyrite films. For example, variations of the sulfur vapor pressure or sulfuration temperature and time (while fixing all others growth parameters) will result in stoichiometric and crystallization differences that subsequently can be correlated to some of the film macroscopic properties[36]. On the other hand, the important role of the substrate where thin films grow has been highlighted in relation to its chemical stability at high temperatures. Diffusion processes of certain elements through the pyrite films may be activated [25]. These phenomena are especially critical when dealing with sodalime

5

glass (SLG) substrates, a very extended substrate type due to its transparency (very useful for accomplishing optical characterization), its thermal linear expansion coefficient that is quite similar to that of pyrite ($\sim 10^{-5}$ K^{-1} in the range 50°–300 °C), and its low cost. In particular, it has been shown that sodium diffusion from the SLG substrate into the pyrite film depends on its sulfuration temperature [25] and that it might affect several of the film properties. For example, the pyrite film doping[15], its structural properties, such as the inhibition of marcasite growth in favor of pyrite [29,37], the existence of amorphous sulfur-deficient secondary phases [24], etc. These important influences of sodium have been also investigated by adding a Na-based precursor [24] or a Na thin film [29] to the sample to be sulfurated deposited on a Na free substrate.

To get a better understanding of the formation mechanism of pyrite films by sulfuration of iron thin films we have investigated their inner profiles. To this end, we have applied transmission electron microscopy (TEM) and related electron energy loss spectroscopy (EELS). Two types of substrates (sodalime glass and amorphous quartz) have been investigated in order to identify the role of some contaminants, particularly, of sodium in the pyrite formation process. We have found that the obtained pyrite thin films are not homogeneous but formed by two parallel layers that differ in thickness, granular distribution, stoichiometry, and impurity content. Surprisingly, we have found that regardless of the substrate, the pyrite layer in direct contact with the substrate presents a highly porous morphology because it is formed by bunches of grains separated by large volumes of empty space. Based on this experimental fact and on a wide structural and chemical characterization of the films grown at different sulfuration temperatures, we have outlined the basis of a formation process of the pyrite thin films by sulfuration of Fe films where the Kirkendall effect must play an important role.

6

2. Experimental Section.

Fe metallic films of thickness between 80 and 200 nm were deposited by thermal evaporation (Edwards E306 A) of Fe powder (Goodfellow, 99.9%) located in a tungsten crucible. Sodalime glass (SLG) substrates were obtained by cutting some microscope slides from Linea LAB (Menzel-Gläser) in small pieces ($26 \times 10 \times 1$ mm^3). In addition, free sodium amorphous quartz substrates (SPI Supplies) of the same dimensions as those of SLG were used for comparison purposes. Before metallic Fe deposition, the substrates were washed with water and neutral soap, rinsed with deionized water and afterwards cleaned with ethyl alcohol (ethanol). These steps were accomplished with the substrates container inside an ultrasonic water bath. A warm and clean airflow was applied to dry all substrates. Before Fe deposition, substrates were kept at 200 °C during 2 h in high vacuum conditions inside the deposition chamber to finish their cleaning. Subsequently, the obtained Fe thin films were sulfurated in a glass ampoule previously sealed under a vacuum of 10^{-6} mbar containing sulfur powder. The amount of sulfur inside the ampoules was the necessary one to reach the sulfur equilibrium vapor pressure at the corresponding sulfuration temperature. The sulfuration of Fe films was performed by heating the glass ampoule up to the sulfuration temperature (T_s), where the sample was kept for 20h and then cooled down to room temperature at its natural rate. Sulfuration temperatures between 250 and 450 ºC have been used for different films. The sample is situated at the hot side of the glass ampoule (T_s), while the sulfur is placed at the other ampoule end, which during the cooling step reaches a temperature that is 15–20 °C lower than that of the hot end, preventing sulfur condensation on the thin film (see Figure SI 1 of the Supporting Information (SI)).

7

Additional details regarding the preparation of pyrite thin films by sulfuration of iron films can be found elsewhere [35].

Structural characterization of the pyrite thin films has been performed by X-ray diffraction (XRD) with an X'Pert PRO Theta/2Theta Panalytical diffractometer in grazing incidence configuration using Cu K_α radiation (CuK_α=1.5406 Å) and an incidence angle of 1.7°. The XRD data were used to calculate the mean crystallite size by using the Scherrer approximation. The morphology of the samples was studied by high-resolution scanning electron microscopy (SEM) and transmission electron microscopy (TEM) images. SEM images were taken with a Dual Beam Helios NanoLab 650 (FEI) equipped with an electron field emission source ElstarTM XHR, operating in a beam energy range between 20-30 keV and a FEI Verios 460 at 2kV of accelerating voltage. These microscopes present a minimum spatial resolution of 0.9 nm and of 0.6 nm, respectively. Lamellas for electron transmission analysis were prepared within the SEM system using a Tomahawk TM ion source of gallium for focused ion beam (FIB) manipulation. The TEM measurements were taken with a FEI Talos F200X equipped with a FEG electron source of 200 keV and with a minimum a resolution of 0.16 nm. Compositional energy dispersive X-ray (EDX) analysis were performed with this same instrument. In addition, chemical characterization was completed by electron energy loss spectroscopy (EELS) studying the Fe-$L_{2,3}$ and S-$L_{2,3}$ edges. The background was removed by a power law expression using Gatan Microscopy Suite (GMS3) software. A Sloan Dektak IIA Profilometer (accuracy ±1 nm) was additionally used to measure the thicknesses of the original metallic samples and those of the sulfurated films.

8

3. Results and Discussion

2.1. Morphology and structure of iron (Fe) thin films

Figures 1 (a) and (b) show the cross-section of two different Fe thin films deposited on glass substrates. Their thicknesses (~134 and ~182 nm, respectively) are quoted in the figure. Both films present a quite similar compact morphology and structure, composed of grains of different shapes and sizes. We here want to emphasize that there is no discontinuity between the substrate and the Fe film and to remark this aspect due to its relevance in the discussion of the results of this investigation. The XRD pattern of an Fe thin film is shown in Figure SI 2 together with others from pyrite films.

2.2. Morphology and structure of pyrite (FeS₂) thin films

The cross-sectional SEM images of pyrite films grown at 300 °C on glass and amorphous quartz substrates are shown in Figure 2 (a) and (b), respectively. Both films are composed by two layers identified as "porous layer" (in contact with the substrate) and "compact layer". The total thickness (porous plus compact layers) of both films are quite similar (~350 nm) and, in particular, the porous layer thickness in each of the films appears to be quite close to the thickness of the original Fe film (~100 nm). The different structure and morphology of both (compact and porous) layers is clearly seen in the figure. Small packets of pyrite grains separated by empty space form the porous layers while the compact ones show very narrow grain boundaries and an almost continuous grain distribution. The results also suggest that the average grain size in the

compact layer is about the same as that in the porous one. As it will be discussed throughout the text, the nature of this bilayer is common to all the prepared films, independent of the respective sulfuration temperature and substrate. Singularly, it appears to be quite independent of the substrate composition and, in particular, of its Na content. X-ray diffraction patterns of the films shown in Figure 2 (c) confirm a non-texturized unique phase corresponding to pyrite (cubic, $Pa\overline{3}$), and no hint of other phases such as pyrrhotite (hexagonal, $P31$, or monoclinic, $A2/a$), marcasite (orthorhombic, $Pnnm$) or iron appear. Equivalent results are obtained for the complete series of samples deposited on glass and sulfurated in the temperature range of 200-450 °C as shown in Figure SI 2. Besides, Figure SI 3 shows the comparison between the normalized XRD peak intensity to that of the (200) peak from Figure SI 2 and those given in the standard ASTM (JCPDS 00-42-1340) card. This comparison confirms that the film crystallization is quite similar to that of the random ASTM FeS_2 polycrystalline samples with no distinct crystallographic texture [25,29,35,36,38–40]. Figure 2d shows a detail of a diffraction pattern of a pyrite crystallite forming a grain (top left insert) from a film sulfurated at 300 °C. As it was said before, only the pyrite phase is identified, confirming the complete structural and chemical transformation of the initial Fe film.

Figure 3 shows TEM images of pyrite lamellas from films deposited on SLG and amorphous quartz sulfurated at different temperatures. The left column gives an overview of the complete thin film. The red and green rectangles in the figures correspond to the porous and compact layers shown, respectively, in the central and right columns. It is clear that the pyrite grains are randomly distributed in all cases, in agreement with the polycrystalline nature of the films shown in the previous X-ray diffraction patterns. Furthermore, we want to point out that the election of these three

10

temperatures (300, 350 and 450 °C) is appropriated because those samples show some interesting phenomena. In the first place, a change of the morphology of the porous layer is clearly seen when comparing the films obtained at 300 °C and 350 °C. The last one presents a denser stripe around the middle of the porous layer, whereas the compact layers of both films seem to remain quite similar. Secondly, on moving to the 450 °C film the size of the grains in the compact layer suffers a significant increment (of around 150% with respect to the former films), which seems to induce a not so compact top layer, with small voids between grains. However, the most astonishing feature is again the formation of the porous layer in contact with the substrate, independent of the particular choice of substrate, here glass or amorphous quartz (as shown formerly in Figure 2), or sulfuration temperature. Taking a closer look at this porous layer, it is clear that it is formed by bunches of grains with a size that is similar to that of the grains in the compact layer. As already noted, they are separated by empty volumes, justifying the denomination "porous layer". Nevertheless, these bunches of grains are connected by what appears an amorphous phase, resulting in a very surprising strong adhesion of the film to the substrate. We tried to detach several films from their substrate by using Scotch® tape, and only small portions of a few of them were removed (same experience was repeated with the initial metallic Fe films with equivalent results). Figure SI 4 shows some fragments of pyrite films removed from glass substrates. Amorphous phases have previously been observed by TEM as located at the boundaries of the pyrite grains [24]. We would like to remark that the presence of this amorphous phase in the porous layer is independent of the chosen substrate, and therefore, of the presence of some impurities like Na. In principle, this situation is different to that reported previously [24], where a sodium pretreatment applied before the sulfuration could eliminate the amorphous secondary phase present around the grain boundaries.

One additional and significant morphological issue is related to the thicknesses of the pyrite films and their layers when compared to the thickness of the initial Fe layers. Taking into account the density, molecular weight and chemical composition of pure Fe and pyrite, the complete sulfuration of an Fe thin film of constant area will turn it into a pyrite film ~3.45 times thicker than the Fe one (no consideration about the film crystallization has been done in this calculation). Figure 4 (a) shows the thicknesses of the two layers forming the pyrite thin films deposited on glass and their sum, i.e., the film total thickness, beside that of the initial Fe layer. In the first place, we note that the total thickness of the film sulfurated at 250 °C is slightly lower than the calculated value (dashed lines in the figure). The opposite happens at the higher sulfuration temperatures (350 °C and 450 °C). These discrepancies are probably related to the crystallization of the pyrite films, as it will be discussed in the following paragraph. But perhaps, the most remarkable fact in the Figure 4a is the similarity between the porous layer thickness and that of the original Fe film. All those characteristics appear to be independent of the substrate used to grow the pyrite films. In Figure 4b, experimental data from pyrite films deposited on glass and amorphous quartz at two different sulfuration temperatures are presented. For a better and easier comparison, we have selected Fe films of the same thickness for both substrates at the same sulfuration temperature (open circles in Figure 4b). The thicknesses of the two layers forming the films are quite similar for both substrates at each sulfuration temperature and, similarly, the total thickness of the films at the same T_s. It is worthwhile to note again that the porous layers of the pyrite films that have evolved on quartz after sulfuration also exhibit thicknesses that are quite similar to those of the Fe films before their sulfuration. Figure 4c shows the relative thickness (thickness of the sulfurated film/ thickness of the original Fe film) of samples on glass as a function of their sulfuration temperature in a

12

wide range of values. Results obtained by applying conventional techniques (profilometry) are compared to data from TEM observations. The relative thickness is temperature dependent for the lower sulfuration temperatures and remains almost constant for $T_s \gtrsim 350°C$. In this temperature range profilometry yields higher values than those from TEM images and also higher than the calculated ones (dashed lines) when $T_s \geq 300°C$

The observed deviation of the film relative thickness from its calculated value was already reported [25] and just explained as a consequence of the pyrite film recrystallization taking place between T_s of 350 °C and 400°C. No knowledge of the formation of porous and compact layers was then available. The current TEM cross-sectional images offer a new explanation in addition to the pyrite recrystallization: the formation of a porous layer with voids will induce a larger thickness of the pyrite film than that expected for a compact one. Additionally, we note that TEM images of the compact layer shown in Figure 3 illustrate how for high sulfuration temperatures (≈450°C) the well-formed pyrite grains leave some empty space between some of their boundaries (compared to lower temperatures), which would induce an even larger deviation of the relative film thickness. Therefore, we may summarize this point by saying that at least two factors may contribute to increase the relative thickness of the films: their crystallization improvement on increasing T_s (due to the grain size increase) and the formation of a porous layer with a thickness very similar to that of the initial Fe film.

Figure 5 shows the crystallite and grain size of the films as a function of their sulfuration temperature. Grain sizes have been determined from TEM images; average values from samples on both substrates are given. The grain size values reported in

13

Figure 5 are from both the compact and the porous layers of the films. No significant difference of that parameter was found between them. In addition, we note that no relevant influence of the substrate type was observed. Results from [41] are also plotted for comparison purposes. We must note, however, that the grain size values reported by Ares et al. (obtained by AFM observations) are from the film surface while in our measurements we were able to probe the bulk of the films with improved statistics. Crystallite sizes were determined from the XRD patterns by applying the Scherrer formalism to several of the diffraction peaks and from TEM data.

2.3. Stoichiometry and impurities: influence of the substrate

Up to this point, we have shown and discussed a set of characteristics of the pyrite films that is common to all of them, independent of the particular choice of substrate used to grow the films. Instead, the most significant experimental parameter appears to be the sample sulfuration temperature.

However, important differences from the compositional point of view have been found between pyrite films grown on quartz and on SLG substrates. Figure 6 shows the TEM-EDX mapping of a sample on amorphous quartz sulfurated at 300 °C. Only Fe, S and O were detected. The average of the atomic composition has been estimated for the compact (table on the left) and for the porous layers (table on the right). In the first place, we note that the concentration of oxygen is larger in the porous region than in the compact one (~18% and ~2.5% atomic concentration, respectively). TEM lamellas have been exposed to the ambient atmosphere during their transportation from the SEM instrument to the electron transmission microscope, so a partial oxidation of the lamella is expected. Oxygen contamination from the substrate must be disregarded due to the thermal stability of quartz at the sulfuration temperatures used in this work. Therefore,

the high oxygen concentration in the porous layer must be related to its larger effective area due to the voids separating grains groups. As a consequence, more active sites sensitive to oxidation by air would be present. In relation to the contents of sulfur and iron of both zones, the compact layer shows a ratio S/Fe ~2.2, slightly higher than the expected stoichiometric ratio of 2.0 for pyrite. However, this ratio rises to ~2.8 in the porous layer, indicating a significant excess of sulfur. Moving towards the films on SLG substrates, Figure 7 shows the equivalent TEM-EDX measurements taken on a sample sulfurated at the same conditions as the previous one ($T_s = 300°C$). As before, the compact layer presents a stoichiometry similar to that of pure pyrite (S/Fe ~2.2) with limited traces of Na (~3%) and O (~5%), while the porous layer presents important deviations. Here, the S/Fe ratio is about 3.7, the O content increases up to ~ 40% and that of Na up to ~20%, i.e., almost 60% of the material contained in the porous layer is not atomically constituted by the chemical elements that form pyrite. The presence of such amounts of oxygen in the porous layer may only be partially justified by the exposure to air during the lamella transportation, and, therefore, we have considered that the rest (~20%) is due to oxygen diffusion from the glass substrate into the film, an amount quite similar to that of Na.

It is already known [25] that glass containing alkali impurities (such as Na) has a weakened O-Si network: some Si-O-Si bridges are broken, and thus some of the O atoms are located at the free end of separated tetrahedrons (Si-O- non-bridging oxygen atoms), facilitating their high mobility. Simultaneously, Na$^+$ ions located at the central part of this broken network also present high mobility [42–44]. The diffusion of Na and O through the pyrite films coming from the SLG substrate and their effects have been reported in terms of accumulation at the films surface [25], marcasite phase formation

inhibition [29,37] and its influence on the film doping [15]. However, to the best of our knowledge there are no previous works dealing with the Na and O distributions through the cross-section of the sulfurated Fe films. Therefore, we think that the following description will help to understand the chemical and physical processes of the Na and O interaction with pyrite. Figure 8 shows the Na atomic concentration as a function of depth for three pyrite films on SLG substrates obtained at three different sulfuration temperatures: 250, 350 and 450 °C. In all cases, the Na concentration reaches its maximum at the frontier between the porous and the compact layers, subsequently decreasing and stabilizing at ~1-2 % in the compact region. As asserted before, Na mainly accumulates at the boundaries of the pyrite grains and at the voids between them (in both compact and porous layers), seemingly confirming that Na mainly diffuses through the grain boundaries of pyrite [25].

More details regarding the different chemical elements distribution in the films are given in Figures 9a and b. These figures show the EDX scan line across the porous and compact layers for two samples sulfurated at $T_s = 350°C$ on quartz and SLG substrates, respectively (for the sake of simplicity only Na, Fe, and S signals are shown, see Figure SI 5 for the O EDX signal). As can be appreciated in Figure 9b, Na is mainly accumulated in the porous layer decreasing its concentration through the compact one, where it reaches very low values. Moreover, S and Fe concentrations in the two samples follow a very similar behavior: both show two maximum within the porous layer and remain almost constant in the compact one. In the porous layer, the $S/_{Fe}$ ratio (black circle symbol in Figure 9) is ~2 inside the pyrite grains but sharply increases between them. The cause of this sulfur excess cannot be entirely related to the presence of Na, since pyrite grown on quartz also shows a sulfur excess in the space

between grains (see Figure 7b). Additionally, it is clear from Figure 9 that the $S/_{Fe}$ ratio is ~2 in the whole compact layer on both substrates.

In spite of the detected excess of sulfur at the grain boundaries of both layers, the experimental data already presented seem to indicate that well-formed pyrite grains, with an almost stoichiometric $S/_{Fe}$ ratio, constitute the samples. However, some differences in the chemical state of the grains forming both layers have been observed. Figure 10 shows the EELS spectra of the Fe $L_{2,3}$ (a) and S $L_{2,3}$ (b) edges for pyrite grains in the compact and porous layers from samples deposited on SLG and quartz substrates sulfurated at 300 °C. The spectral shapes of the respective S and Fe edges are almost equivalent for both layers and substrates, corresponding to pyrite [45]. However, the porous layer Fe $L_{2,3}$ edge shows small differences between the sample on SLG and that on quartz. Figure SI 6 shows the spin-orbital separation between the Fe $2p_{3/2}$ and $2p_{1/2}$ contributions (ΔE Fe$L_{2,3}$) and the intensity ratio of both contributions. The two parameters behave as expected when signals from the compact layer are considered (ΔE Fe$L_{2,3}$ is very close to the typical value of ~12.05 eV and the intensity ratio is around 2). However, for the porous layer we see a considerable difference between the values of both parameters depending on the sample substrate. The films grown on quartz behave as expected; however, the porous layer of the film on SLG yields values of both parameters, which are much higher than the expected ones. These two variations indicate that an enhanced oxidation of the pyrite grains in the porous layer of the sample on the SLG substrate has taken place [46]. This result agrees with those from EDX analysis already presented, which showed a high oxygen concentration in the porous layer of the film deposited on glass.

It was shown before that even for the compact layer the average chemical

17

composition of a large area showed an excess of sulfur. This is in line with the results from EDX measurements, which give an average for the whole film. In addition, S 2p X-ray photoelectron spectroscopy (XPS) spectra showed similar surface results from samples grown by this sulfuration route [25], regardless possible sulfur condensation on their surface during the cooling process [47]. It was then proposed that the excess of sulfur was mainly formed by sulfur with a coordination number different to that presented in FeS_2 or even to unbounded sulfur or polysulfides. This behavior of sulfur has been reported to occur in pyrite thin films on both SLG and Na-free substrates (amorphous quartz and alumina) [25,48,49]. Thus, our present results seem to suggest that this excess of sulfur is due to some intrinsic process closely related to the formation reactions of the pyrite thin films. As has been shown, the sulfur excess is concentrated along the grain boundaries of the polycrystalline thin films while the grains present a unique pyrite phase with good stoichiometry. The presence of Na diffused from the SLG substrates would promote the fixation of S and the formation of Na-S-O compounds mainly accumulated in the grain boundaries of the porous layer. These experimental facts might explain that the presence of this alkali scarcely affects the macroscopic properties of pyrite thin films.

2.4. Insight on the formation mechanism of pyrite thin films by sulfuration of Fe thin films

The formation mechanism of pyrite thin films is still an open question. In part, this is due to that many synthesis routes can be followed and the final morphological, structural, etc. characteristics of the films will depend on the selected experimental parameters in each one of the growth methods. Focusing on the sulfuration of Fe thin films, we have shown in this work that the pyrite films have a complex bilayer morphology. This finding might give worthy information about the pyrite formation

mechanism by sulfuration of Fe films.

A common feature to all the films sulfurated at different temperatures on either SLG or amorphous quartz substrates is the formation of what we have called the porous layer in contact with the substrate and with a thickness that is quite similar to that of the initial Fe film. This layer has a few grain groups within an extended empty volume. The formation of these localized voids in the porous layer must be the result of the Fe sulfuration process. In fact, nothing similar has been seen to exist in the Fe films before their sulfuration, see Figure 1. This experimental finding clearly suggests that some variation of the Kirkendall effect is active during the sulfuration: the diffusion of iron atoms from the film bulk to its surface is accompanied by diffusion of Fe vacancies in the opposite sense [50]. According to the work presented by Smigelkas and Kirkendall [51], the differences on the diffusivities of the different components in a diffusion couple (classically two metals) may lead to the formation of voids in the region occupied by that material of higher diffusivity. The larger flow of matter in one direction is balanced by an opposite flow of vacancies, which may condense in the form of voids. This basis has been extended to solid/gas or solid/liquid interfaces and, in particular, to the formation of oxides and sulfides of metals. Particularly, the Kirkendall effect at the nanoscale was first explored by Alivisatos and co-workers to synthesize hollow nanostructures based on Co oxides, sulfides and selenides [52]. More recently, this approach has been extended to other materials as Pb [53] and Fe, in the last case to achieve FeS nanotubes from hematite nanorods after a sulfuration process carried out with H_2S [54]. These examples show that the Kirkendall effect may play an important role in the formation of pyrite films by sulfuration of Fe films.

In the current work, we have only presented a schematic and very qualitative description of the processes that may contribute to the Fe film transformation into a

pyrite film. However, based on the former experimental results, we are just trying to elaborate a full formulation of the reactions taking place during the growth of a pyrite film [55]. The basis of this formulation are the following: the S_2 molecules in the sulfur vapor ionizes in S^{2-} at the surface of the metallic film and react with Fe, firstly forming a monosulfide ($Fe_{1-x}S$, pyrrhotite) layer [55]. The work from A. Pascual et al. shows the existence of these intermediate phases (hexagonal and orthorhombic pyrrhotite) by stopping the sulfuration process at different times, and by in-situ study of the phase transition effects on the transport properties of the films [36]. Besides, by this same experimental method different sulfuration degrees can be obtained by controlling the kinetics of the monosulfide to disulfide reaction step, as shown in [25,36,56], what makes pyrrhotite a hard phase to detect except for very well determined experimental conditions. Thus, during this first step of the reaction, the observed Kirkendall effect (the porous layer formation) would be due to a significant difference of the diffusion rates of the iron of the original film and the sulfur ions in the surrounding atmosphere. This unequal diffusivity leads to the formation of voids at the Fe film-substrate interface that gradually increase in size as the reaction takes place. As shown, this process is independent of the substrate (reflected here for glass and quartz substrates, selected by their different interaction with the film in terms of elemental diffusion [15]). Besides, the thickness of the porous layer allows discarding a substrate-layer interaction effect to explain the presence of this porous layer. Finally, the initial compact morphology of our polycrystalline metallic iron film also dismisses a direct evolution of voids from the as deposited layer, as it may occur with other deposition methods, as spray pyrolysis [57] or spin coating [24].

Once the Fe is completely transformed into $Fe_{1-x}S$, the sulfuration process leads to a full conversion of this monosulfide into the pyrite phase, FeS_2 [36,55]. Gradually,

20

the empty layer could collapse and be partially filled with pyrite grains forming the porous layer (with very similar thickness to that of the initial metallic film). Besides, due to the high temperatures (>200 °C) and times (20h) of the sulfuration process, some grains would aggregate improving the adherence of the film to the substrate. The S excess at the grain boundaries could be well justified because of the S diffusion precisely through the boundaries, leading to the amorphous phase formed by polysulfide, S-rich $Fe_{1-x}S$ species or even unbounded sulfur. On the other hand, the higher concentration of S at the porous layer could be explained due to its reaction with other elements forming S-O and S-Na-O compounds (depending on the substrate). As pointed out previously [25], the Na diffusion could be activated once the Fe is sulfurated. A very similar trend will follow the O atoms diffused from the substrate to form some amorphous phase of S-Na-O based compounds at the boundaries of the voids.

4. Conclusions

The synthesis of pyrite films by sulfuration of Fe films appears to be a straightforward experimental process; however, it seems to be very complex from a chemical point of view. The present investigation provides a description of the pyrite thin films obtained at different sulfuration temperatures and deposited on different substrates. New hints to understand the synthesis process have been provided, enabling an increased control of the film bulk properties. TEM cross-sectional images show some common features to all films, independently of their sulfuration temperature and the elected substrate: 1) the pyrite films are composed by two layers, one more compact and thicker and a second one, which is quite porous, in contact with the substrate and with a thickness similar to that of the original Fe thin film. The grains of both layers are almost

equal in terms of size, stoichiometry, and structure, supporting the idea of a common formation process. 2) the pyrite films present an excess of sulfur, which is localized at the grain boundaries. Both findings support the proposal that the Fe sulfuration process induces the formation of a porous layer may be regarded as a manifestation of the Kirkendall effect operating in the synthesis of pyrite thin films in the range of hundreds of nanometers. In addition, the distribution of sodium and oxygen diffused from the glass substrates into the pyrite films has been investigated, what led us to conclude that the porous layer acts as a physical barrier reducing the O and Na concentration in the compact layer. Sodium that mainly diffuses through the film grain boundaries barely dopes the pyrite grains and, hence, reduces its influence on the macroscopic properties of the film.

In the light of our present results, some very interesting questions remain unanswered or even just suddenly appear. Perhaps the most pertinent of these questions is that a future elaboration of a model of the formation mechanism of pyrite thin films should address processes that would lead to the appearance of the Kirkendall effect. At the same time, the so far hidden porous layer might significantly affect the transport properties (electrical and thermal) and other macroscopic parameters (such as optical ones) of pyrite thin films. Conseqently, future work should elucidate the influence of this porous layer on the pyrite thin film properties, which might be relevant for a selected application of interest.

Declaration of interests

☒ The authors declare that they have no known competing financial interests or personal relationships that could have appeared to influence the work reported in this paper.

☐ The authors declare the following financial interests/personal relationships which may be considered as potential competing interests:

Acknowledgements

References

[1]   K.P. Bhandari, P. Koirala, N.R. Paudel, R.R. Khanal, A.B. Phillips, Y. Yan, R.W. Collins, M.J. Heben, R.J. Ellingson, Iron pyrite nanocrystal film serves as a copper-free back contact for polycrystalline CdTe thin film solar cells, Sol. Energy Mater. Sol. Cells. 140 (2015) 108–114. https://doi.org/10.1016/j.solmat.2015.03.032.

[2]   Z. Shi, A.H. Jayatissa, F.C. Peiris, Fabrication of semiconducting pyrite thin films from hydrothermally synthesized pyrite (FeS2) powder, J. Mater. Sci. Mater. Electron. 27 (2016) 535–542. https://doi.org/10.1007/s10854-015-3786-5.

[3]   A. Walimbe, A. Wertheim, A. Ravi, C. Kopas, A. Saxena, R.K. Singh, S.W. Lehner, J. Domenico, J. Makar, R.W. Carpenter, P.R. Buseck, N. Newman, Influence of substrate temperature on properties of pyrite thin films deposited using a sequential coevaporation technique, Thin Solid Films. 669 (2019) 49–55. https://doi.org/10.1016/j.tsf.2018.10.022.

[4]   T. Van Nguyen, N.T.N. Truong, P. Ho, T.K. Trinh, J.H. Kim, C. Park, Green and simple preparation of carbon-coated iron pyrite thin films for solar cells application, J. Mater. Sci. Mater. Electron. 30 (2019) 19752–19759. https://doi.org/10.1007/s10854-019-02340-7.

[5]   R.P. Srivastava, S. Ingole, An investigation on the phase purity of iron pyrite (FeS2) thin films obtained from the sulfurization of hematite (Fe2O3) thin films, Mater. Sci. Semicond. Process. 106 (2020) 104775. https://doi.org/10.1016/j.mssp.2019.104775.

[6]   D. Wan, Y. Wang, Z. Zhou, G. Yang, B. Wang, L. Wei, Fabrication of the ordered FeS2 (pyrite) nanowire arrays in anodic aluminum oxide, Mater. Sci. Eng. B. 122 (2005) 156–159. https://doi.org/10.1016/j.mseb.2005.05.003.

[7]   Y. Bai, J. Yeom, M. Yang, S.-H. Cha, K. Sun, N.A. Kotov, Universal Synthesis of Single-Phase Pyrite FeS2 Nanoparticles, Nanowires, and Nanosheets, J. Phys. Chem. C. 117 (2013) 2567–2573. https://doi.org/10.1021/jp3111106.

[8]   H. Qin, J. Jia, L. Lin, H. Ni, M. Wang, L. Meng, Pyrite FeS2 nanostructures: Synthesis, properties and applications, Mater. Sci. Eng. B. 236–237 (2018) 104–124. https://doi.org/10.1016/j.mseb.2018.11.003.

[9]   G. Kaur, M. Kaur, A. Thakur, A. Kumar, Recent Progress on Pyrite FeS2 Nanomaterials for Energy and Environment Applications: Synthesis, Properties and Future Prospects, J. Clust. Sci. (2019). https://doi.org/10.1007/s10876-019-01708-3.

[10] I.J. Ferrer, D.M. Nevskaia, C. de las Heras, C. Sánchez, About the band gap nature of FeS2 as determined from optical and photoelectrochemical measurements, Solid State Commun. 74 (1990) 913–916. https://doi.org/10.1016/0038-1098(90)90455-K.

[11] C. De las Heras, I.J. Ferrer, C. Sanchez, Temperature dependence of the optical absorption edge of pyrite FeS2 thin films, J. Phys. Condens. Matter. 6 (1994) 10177.

[12] S. Fiechter, J. Mai, A. Ennaoui, W. Szacki, Chemical vapour transport of pyrite (FeS2) with halogen (Cl, Br, I), J. Cryst. Growth. 78 (1986) 438–444. https://doi.org/10.1016/0022-0248(86)90144-2.

[13] G. Chatzitheodorou, S. Fiechter, M. Kunst, J. Luck, H. Tributsch, Low temperature chemical preparation of semiconducting transition metal chalcogenide films for energy conversion and storage, lubrication and surface protection, Mater. Res. Bull. 23 (1988) 1261–1271. https://doi.org/10.1016/0025-5408(88)90114-6.

[14] I.J. Ferrer, F. Caballero, C.D. las Heras, C. Sánchez, Preparation of n-type doped FeS2 thin films, Solid State Commun. 89 (1994) 349–352. https://doi.org/10.1016/0038-1098(94)90598-3.

[15] E. Flores, S. Yoda, C. Morales, O. Caballero-Calero, P. Díaz-Chao, M. Martín-González, J.R. Ares, I.J. Ferrer, C. Sánchez, Pyrite thin films on amorphous substrates: Interaction with the substrate and doping effects, Thin Solid Films. 672 (2019) 138–145. https://doi.org/10.1016/j.tsf.2019.01.020.

[16] M. Limpinsel, N. Farhi, N. Berry, J. Lindemuth, C.L. Perkins, Q. Lin, M. Law, An inversion layer at the surface of n-type iron pyrite, Energy Environ. Sci. 7 (2014) 1974–1989. https://doi.org/10.1039/C3EE43169J.

[17] S. Uchiyama, Y. Ishikawa, Y. Uraoka, Effect of inversion layer at iron pyrite surface on photovoltaic device, Jpn. J. Appl. Phys. 57 (2018) 032301. https://doi.org/10.7567/JJAP.57.032301.

[18] M. Cabán-Acevedo, N.S. Kaiser, C.R. English, D. Liang, B.J. Thompson, H.-E. Chen, K.J. Czech, J.C. Wright, R.J. Hamers, S. Jin, Ionization of High-Density Deep Donor Defect States Explains the Low Photovoltage of Iron Pyrite Single Crystals, J. Am. Chem. Soc. 136 (2014) 17163–17179. https://doi.org/10.1021/ja509142w.

[19] X. Zhang, M. Manno, A. Baruth, M. Johnson, E.S. Aydil, C. Leighton, Crossover From Nanoscopic Intergranular Hopping to Conventional Charge Transport in Pyrite Thin Films, ACS Nano. 7 (2013) 2781–2789. https://doi.org/10.1021/nn4003264.

[20] X. Zhang, M. Li, J. Walter, L. O'Brien, M.A. Manno, B. Voigt, F. Mork, S.V. Baryshev, J. Kakalios, E.S. Aydil, C. Leighton, Potential resolution to the doping puzzle in iron pyrite: Carrier type determination by Hall effect and thermopower, Phys Rev Mater. 1 (2017) 015402. https://doi.org/10.1103/PhysRevMaterials.1.015402.

[21] J. Walter, X. Zhang, B. Voigt, R. Hool, M. Manno, F. Mork, E.S. Aydil, C. Leighton, Surface conduction in n-type pyrite (FeS2) single crystals, Phys Rev Mater. 1 (2017) 065403. https://doi.org/10.1103/PhysRevMaterials.1.065403.

[22] R.D. McAuliffe, D.P. Shoemaker, Inflexible stoichiometry in bulk pyrite FeS2 as viewed by in situ and high-resolution X-ray diffraction, Acta Crystallogr. Sect. B. 74 (2018) 436–444. https://doi.org/10.1107/S2052520618010144.

[23] B. Voigt, W. Moore, M. Manno, J. Walter, J.D. Jeremiason, E.S. Aydil, C. Leighton, Transport Evidence for Sulfur Vacancies as the Origin of Unintentional n-Type Doping in Pyrite FeS2, ACS Appl. Mater. Interfaces. 11 (2019) 15552–15563. https://doi.org/10.1021/acsami.9b01335.

[24] D.G. Moon, T.R. Rana, S. Rehan, S.D. Haider Naqvi, Y. Siddique, S.M. Lee, S.K. Ahn, Y.S. Cho, S. Ahn, Na-Mediated Stoichiometry Control of FeS2 Thin Films: Suppression of Nanoscale S-Deficiency and Improvement of Photoresponse, ACS Appl. Mater. Interfaces. 11 (2019) 43244–43251. https://doi.org/10.1021/acsami.9b16144.

[25] C. Morales, E. Flores, S. Yoda, M.A. Niño, D. [Martín y Marero, L. Soriano, J. Rojo, J.R. Ares, I.J. Ferrer, C. Sánchez, An XPS investigation on the influence of the substrate and growth conditions on pyrite thin films surface composition, Appl. Surf. Sci. 492 (2019) 651–660. https://doi.org/10.1016/j.apsusc.2019.06.214.

[26] G. Chatzitheodorou, S. Fiechter, R. Könenkamp, M. Kunst, W. Jaegermann, H. Tributsch, Thin photoactive FeS2 (pyrite) films, Mater. Res. Bull. 21 (1986) 1481–1487. https://doi.org/10.1016/0025-5408(86)90088-7.

[27] N. Takahashi, T. Sawada, T. Nakamura, T. Nakamura, Preparation of pyrite thin films by atmospheric pressure chemical vapor deposition using FeCl and CHCSNH, J Mater Chem. 10 (2000) 2346–2348. https://doi.org/10.1039/B003015P.

[28] B. Meester, L. Reijnen, A. Goossens, J. Schoonman, Synthesis of Pyrite (FeS2) Thin Films by Low-Pressure MOCVD, Chem. Vap. Depos. 6 (2000) 121–128. https://doi.org/10.1002/(SICI)1521-3862(200006)6:3<121::AID-CVDE121>3.0.CO;2-S.

[29] N. Berry, M. Cheng, C.L. Perkins, M. Limpinsel, J.C. Hemminger, M. Law, Atmospheric-Pressure Chemical Vapor Deposition of Iron Pyrite Thin Films, Adv. Energy Mater. 2 (2012) 1124–1135. https://doi.org/10.1002/aenm.201200043.

[30] D. Susac, L. Zhu, M. Teo, A. Sode, K.C. Wong, P.C. Wong, R.R. Parsons, D. Bizzotto, K.A.R. Mitchell, S.A. Campbell, Characterization of FeS2-Based Thin Films as Model Catalysts for the Oxygen Reduction Reaction, J. Phys. Chem. C. 111 (2007) 18715–18723. https://doi.org/10.1021/jp073395i.

[31] X. Zhang, T. Scott, T. Socha, D. Nielsen, M. Manno, M. Johnson, Y. Yan, Y. Losovyj, P. Dowben, E.S. Aydil, C. Leighton, Phase Stability and Stoichiometry in Thin Film Iron Pyrite: Impact on Electronic Transport Properties, ACS Appl. Mater. Interfaces. 7 (2015) 14130–14139. https://doi.org/10.1021/acsami.5b03422.

[32] A. Yamamoto, M. Nakamura, A. Seki, E.L. Li, A. Hashimoto, S. Nakamura, Pyrite (FeS2) thin films prepared by spray method using FeSO4 and (NH4)2Sx, Sol. Energy Mater. Sol. Cells. 75 (2003) 451–456. https://doi.org/10.1016/S0927-0248(02)00205-2.

[33] P. Ho, T.N. Van, J.H. Lee, Y.J. Jang, R. Cheruku, C. Park, K.-S. Ahn, J.H. Kim, Shape Control Iron Pyrite Synthesized by Hot Injection Method: Counter

Electrode for Efficient Dye-Sensitized Solar Cells, Electron. Mater. Lett. 15 (2019) 350–356. https://doi.org/10.1007/s13391-019-00140-z.

[34] S. Nakamura, A. Yamamoto, Electrodeposition of pyrite(FeS2) thin films for photovoltaic cells, Sol. Energy Mater. Sol. Cells. 65 (2001) 79–85. https://doi.org/10.1016/S0927-0248(00)00080-5.

[35] I.J. Ferrer, C. Sánchez, Characterization of FeS2 thin films prepared by thermal sulfidation of flash evaporated iron, J. Appl. Phys. 70 (1991) 2641. https://doi.org/10.1063/1.349377.

[36] A. Pascual, S. Yoda, M. Barawi, J.M. Clamagirand, J.R. Ares, I.J. Ferrer, C. Sánchez, Iron Pyrite from Iron Thin Films: Identification of Intermediate Phases and Associated Conductivity-type Transitions, J. Phys. Chem. C. 118 (2014) 26440–26446. https://doi.org/10.1021/jp505303d.

[37] S. Seefeld, M. Limpinsel, Y. Liu, N. Farhi, A. Weber, Y. Zhang, N. Berry, Y.J. Kwon, C.L. Perkins, J.C. Hemminger, R. Wu, M. Law, Iron Pyrite Thin Films Synthesized from an Fe(acac) $_3$ Ink, J. Am. Chem. Soc. 135 (2013) 4412–4424. https://doi.org/10.1021/ja311974n.

[38] X. Zhang, M. Li, J. Walter, L. O'Brien, M.A. Manno, B. Voigt, F. Mork, S.V. Baryshev, J. Kakalios, E.S. Aydil, C. Leighton, Potential resolution to the doping puzzle in iron pyrite: Carrier type determination by Hall effect and thermopower, Phys Rev Mater. 1 (2017) 015402. https://doi.org/10.1103/PhysRevMaterials.1.015402.

[39] I.J. Ferrer, C. De Las Heras, N. Menéndez, J. Tornero, C. Sánchez, Application of Mössbauer spectroscopy to study the formation of iron pyrite thin films, J. Mater. Sci. 28 (1993) 389–393. https://doi.org/10.1007/BF00357814.

[40] C. de las Heras, C. Sanchez, Characterization of iron pyrite thin films obtained by flash evaporation, Thin Solid Films. 199 (1991) 259–267. https://doi.org/10.1016/0040-6090(91)90008-L.

[41] J.R. Ares, A. Pascual, I.J. Ferrer, C. Sánchez, Grain and crystallite size in polycrystalline pyrite thin films, EMRS 2004. 480–481 (2005) 477–481. https://doi.org/10.1016/j.tsf.2004.11.064.

[42] W.H. Zachariasen, The atomic arrangement in glass, J. Am. Chem. Soc. 54 (1932) 3841–3851.

[43] F.L. Freire Jr, G.M. Sigaud, Na+ Transport Through Sodium Containing Insulators Under Proton Irradiation, Braz. J. Phys. 23 (1993) 253–258.

[44] S.R. Elliott, Physics of amorphous materials, 2nd ed., Longman Scientific & Technical, USA, 1990. https://books.google.es/books?id=QgtRAAAAMAAJ.

[45] L.A.J. Garvie, P.R. Buseck, Unoccupied states of pyrite probed by electron energy-loss spectroscopy (EELS), Am. Mineral. 89 (2004) 485–491. https://doi.org/10.2138/am-2004-0402.

27

[46] H. Tan, J. Verbeeck, A. Abakumov, G. [Van Tendeloo, Oxidation state and chemical shift investigation in transition metal oxides by EELS, Ultramicroscopy. 116 (2012) 24–33. https://doi.org/10.1016/j.ultramic.2012.03.002.

[47] N. Hamdadou, A. Khelil, J.C. Bernède, Pyrite FeS2 films obtained by sulphuration of iron pre-deposited films, Mater. Chem. Phys. 78 (2003) 591–601. https://doi.org/10.1016/S0254-0584(01)00577-6.

[48] T.K. Trinh, N.T.N. Truong, V.T.H. Pham, H. Kim, C. Park, Effect of sulfur annealing on the morphological, structural, optical and electrical properties of iron pyrite thin films formed from FeS2 nano-powder, Korean J. Chem. Eng. 35 (2018) 1525–1531. https://doi.org/10.1007/s11814-018-0060-6.

[49] S. Chaturvedi, R. Katz, J. Guevremont, M.A.A. Schoonen, D.R. Strongin, XPS and LEED study of a single-crystal surface of pyrite, Am. Mineral. 81 (1996) 261–264. https://doi.org/10.2138/am-1996-1-234.

[50] J.M. Philibert, Atom movements: Diffusion and mass transport in solids, Les Éditions de Physique, France, 1991.

[51] A.D. Smigelskas, E.O. Kirkendall, Zinc Diffusion in Alpha Brass, Am. Inst. Min. Metall. Eng. (1947) 1–5.

[52] Y. Yin, R.M. Rioux, C.K. Erdonmez, S. Hughes, G.A. Somorjai, A.P. Alivisatos, Formation of Hollow Nanocrystals Through the Nanoscale Kirkendall Effect, Science. 304 (2004) 711–714. https://doi.org/10.1126/science.1096566.

[53] S.S. Mali, J.V. Patil, C.K. Hong, Formation of Kirkendall void of lead-sulfide cubes, Mater. Today. 40 (2020) 266–267. https://doi.org/10.1016/j.mattod.2020.10.001.

[54] D.R. Cummins, H.B. Russell, J.B. Jasinski, M. Menon, M.K. Sunkara, Iron Sulfide (FeS) Nanotubes Using Sulfurization of Hematite Nanowires, Nano Lett. 13 (2013) 2423–2430. https://doi.org/10.1021/nl400325s.

[55] Antonio Pascual, La formación de películas delgadas en sulfuros metálicos investigada mediante medidas in situ de sus propiedades de transporte, PhD Thesis, Universidad Autónoma de Madrid, 2005.

[56] M.A. Niño, E. Flores, C. Sánchez, J.M. Rojo, Reactivity of a FeS Surface under Room Temperature Exposure to Nitrogen and H 2 S, J. Phys. Chem. B. 122 (2018) 705–712. https://doi.org/10.1021/acs.jpcb.7b06309.

[57] B. Ouertani, J. Ouerfelli, M. Saadoun, B. Bessaïs, H. Ezzaouia, J.C. Bernède, Characterization of FeS2-pyrite thin films synthesized by sulphuration of amorphous iron oxide films pre-deposited by spray pyrolysis, Mater. Charact. 54 (2005) 431–437. https://doi.org/10.1016/j.matchar.2005.01.009.
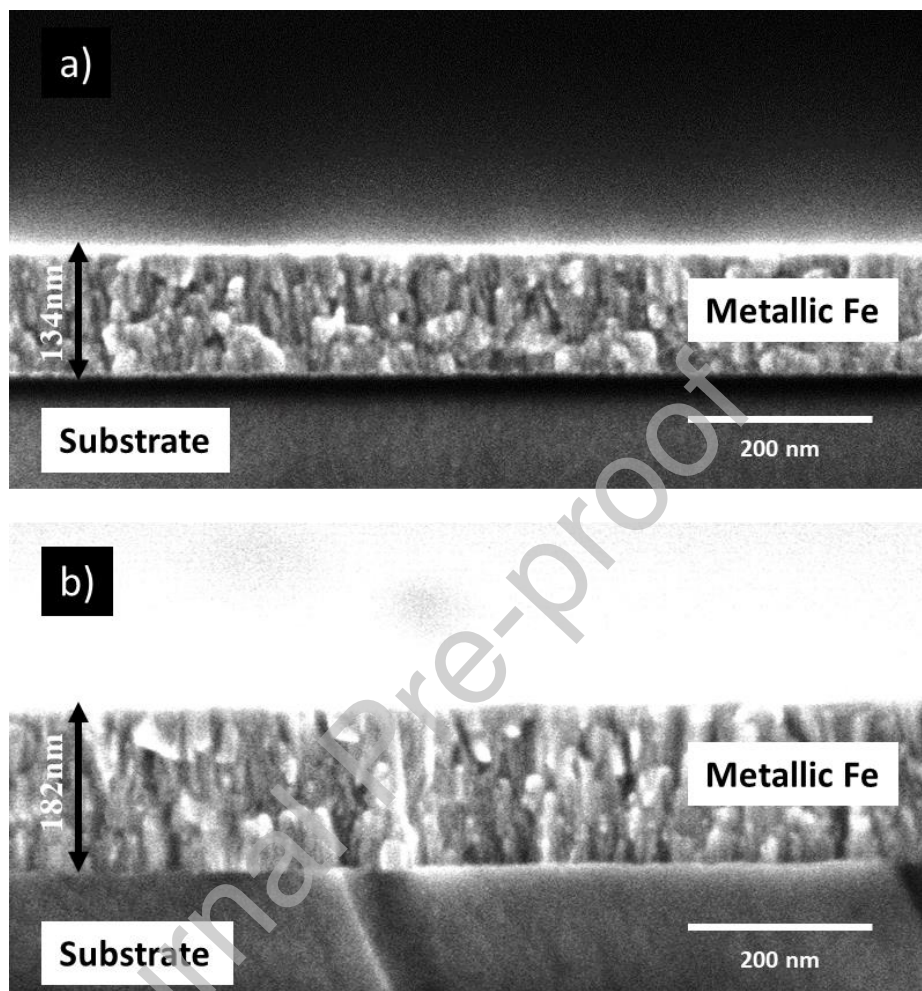
Figure 1.

Figure 1. a) and b) cross-sectional SEM-FEG images of Fe metallic thin films deposited on SLG substrates. Thicknesses of the Fe metallic thin films of a) ~134 nm and b) ~182 nm are given in the images.
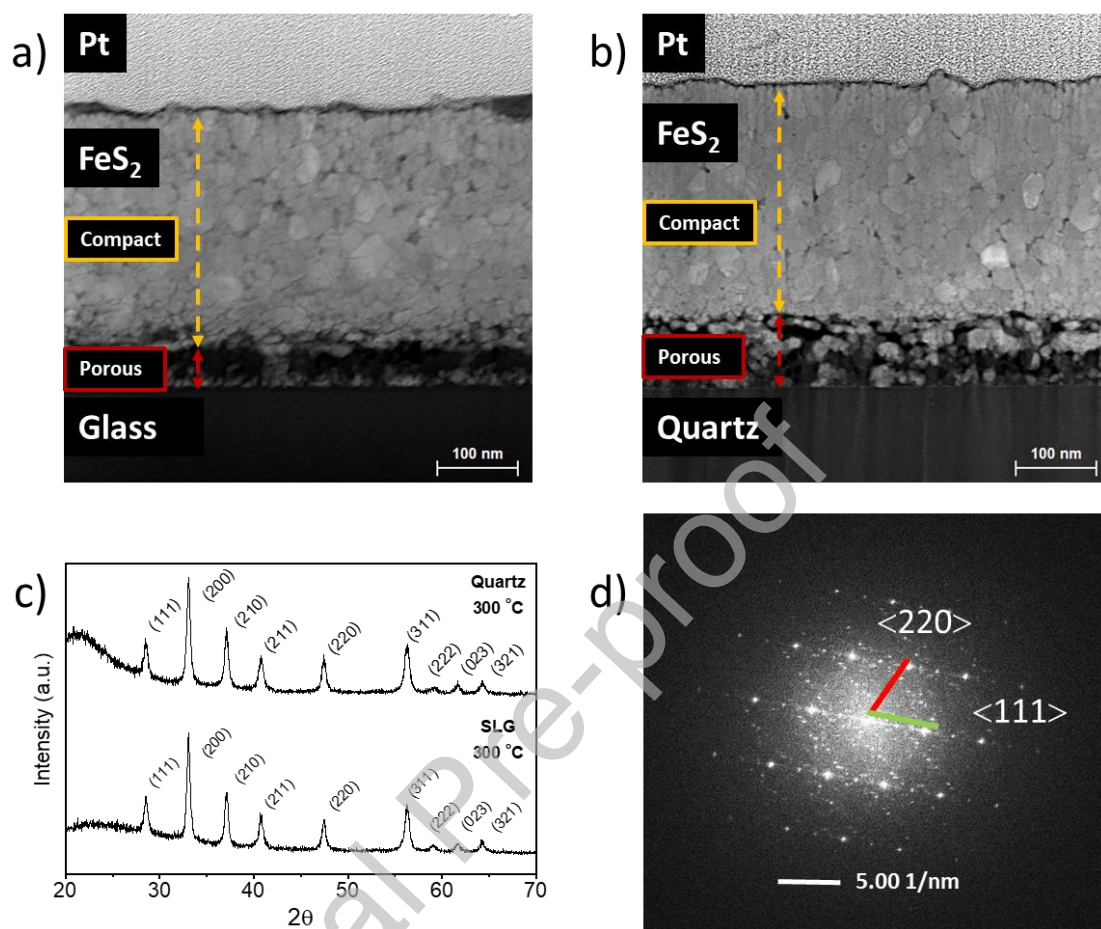
Figure 2.

Figure 2. a) and b) cross-sectional SEM images of pyrite thin films grown at 300 °C on a) SLG and b) quartz substrates, respectively. The two different layers composing the films are indicated by the respective labels. c) X-ray diffraction patterns of pyrite films shown in a) and b). Pyrite diffraction peaks are indicated. d) Diffraction pattern of a single pyrite crystallite (grown on SLG) obtained by TEM, where <220> and <111> orientations are indicated.
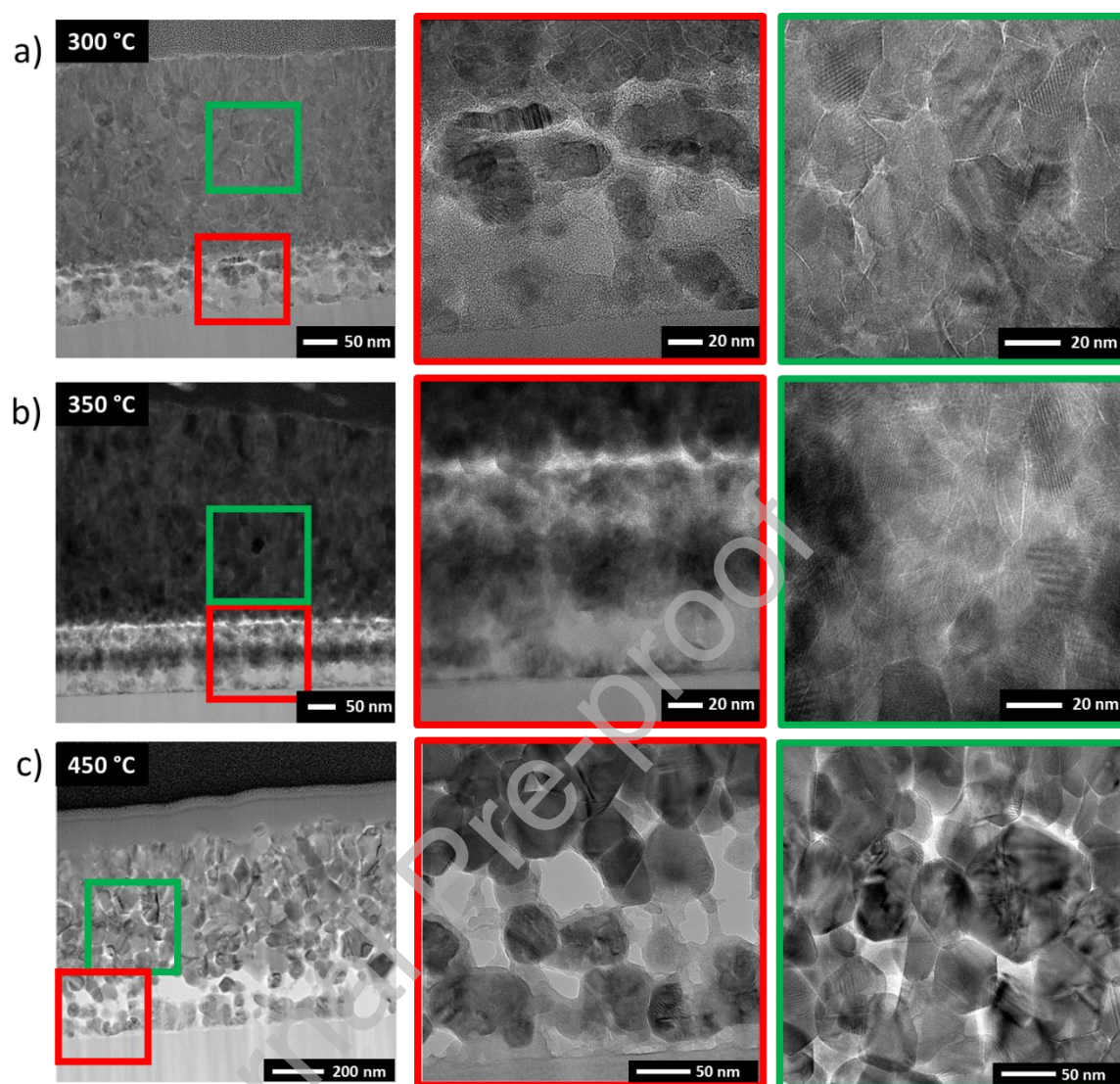
Figure 3.

Figure 3. TEM images of pyrite thin films sulfurated at a) 300 °C on quartz, b) 350 °C on quartz and c) 450 °C on SLG substrates. Left column shows an overview of the whole film, where red and green rectangles indicate the porous and compact layers, which are zoomed in the central and right columns.
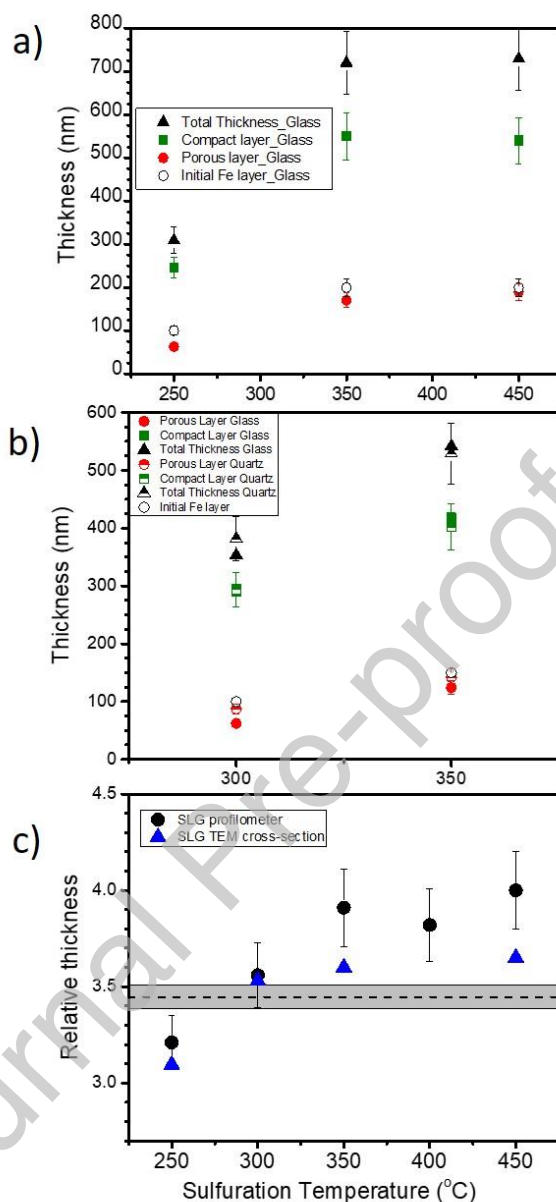
Figure 4.

Figure 4. a) Total thickness of pyrite films (black triangles), thicknesses of compact (green square) and porous (red circle) layers, and initial thickness of Fe films (open circles) as a function of their sulfuration temperatures. b) Samples grown on SLG and quartz substrates are represented by stuff and semi-stuff symbols, respectively. c) Variation of the relative (thickness determined by TEM and profilometry) of sulfurated films on SLG substrates with sulfuration temperature. The dashed line (and their gray background as allowed uncertainty) represents the expected relative thickness of the films.
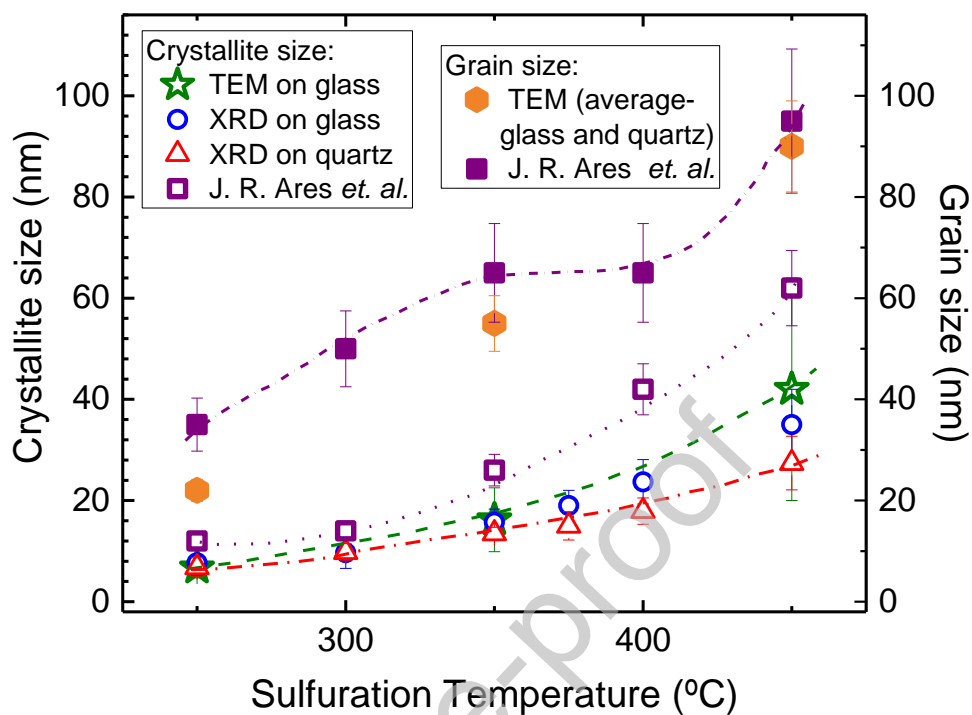
Figure 5.

Figure 5. Crystallite (open symbols) and grain (filled symbols) size of pyrite thin films as a function of the sulfuration temperature estimated by applying the Scherrer formula to the (200) diffraction peak and from TEM images. The corresponding film substrate and the data source are shown in the graph legends. Data from Ares *et.al.* (obtained from XRD and AFM data) are also plotted. The curves in the figures are only a guide for the eyes.

Figure 6

Element	At. Con (%)	Error in % (1 Sigma)
Sulfur	67.0	1.7
Iron	30.6	1.4
Oxygen	2.4	0.1

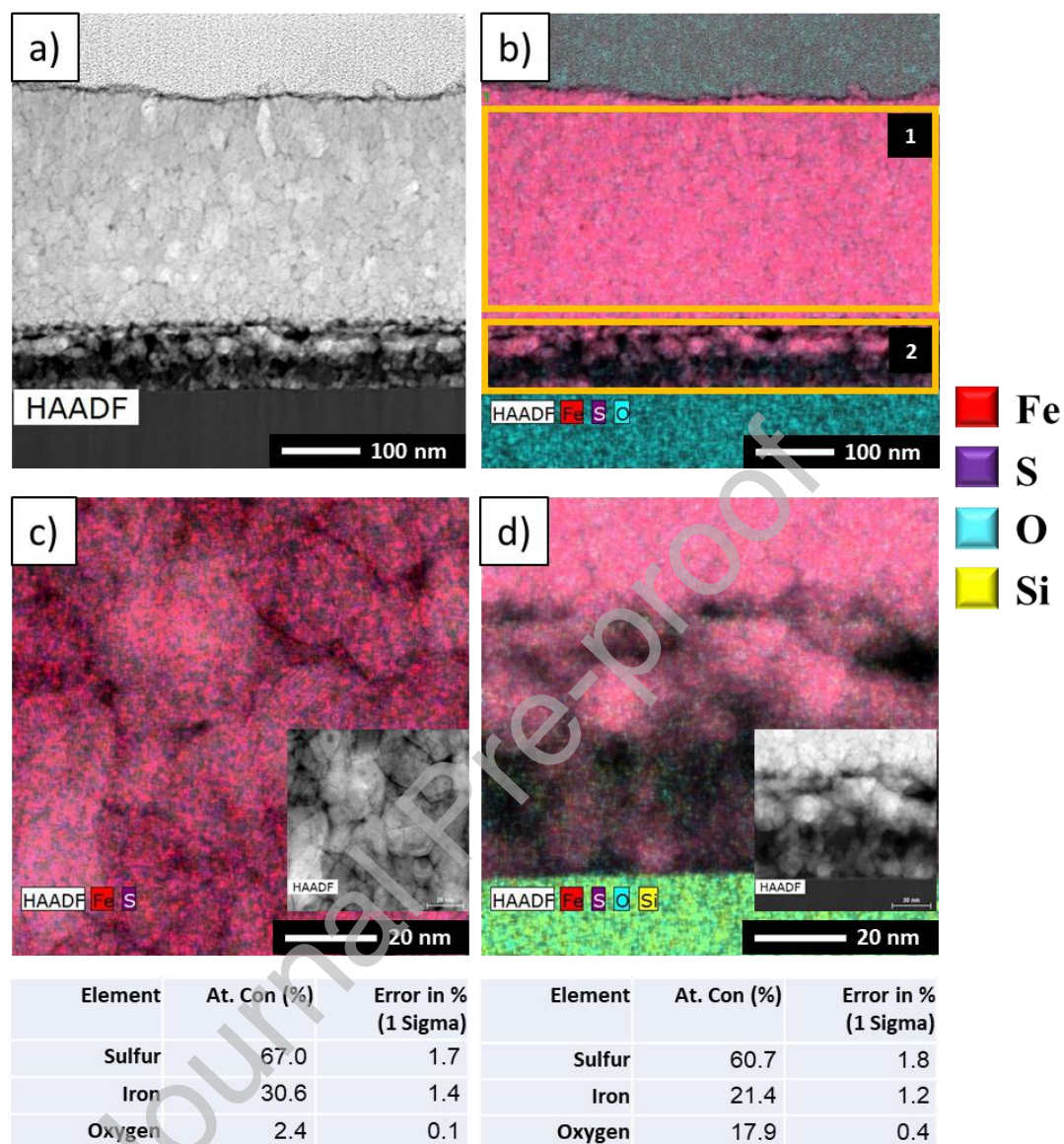| Element	At. Con (%)	Error in % (1 Sigma)
Sulfur	60.7	1.8
Iron	21.4	1.2
Oxygen	17.9	0.4

Figure 6. TEM images of a lamella prepared from an Fe film sulfurated at 300 °C on amorphous quartz. a) General overview of the complete pyrite layer (TEM-HAADF image) and b) same image colored by the overlapped EDX mapping. Orange rectangles delimit the compact (1) and porous (2) layers analyzed by EDX. The corresponding average atomic concentrations are shown in the tables at the bottom: left, compact layer; right, porous layer. c) and d) zoomed TEM-HAADF images of the compact and porous layers colored with the EDX mapping, respectively. Bottom right corner inserts correspond to the original TEM image.
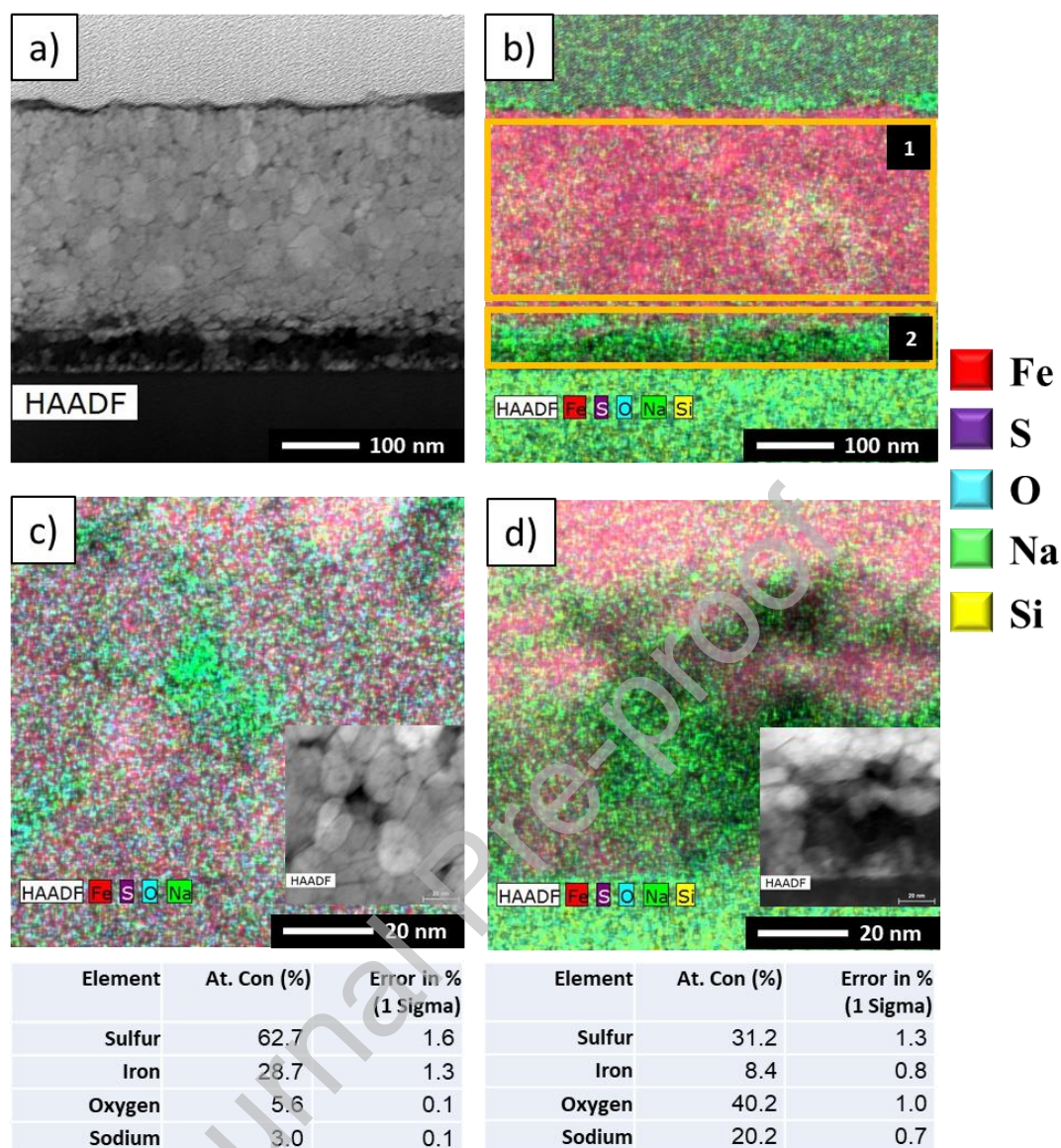
Figure 7

Element	At. Con (%)	Error in % (1 Sigma)
Sulfur	62.7	1.6
Iron	28.7	1.3
Oxygen	5.6	0.1
Sodium	3.0	0.1

Element	At. Con (%)	Error in % (1 Sigma)
Sulfur	31.2	1.3
Iron	8.4	0.8
Oxygen	40.2	1.0
Sodium	20.2	0.7

Figure 7. TEM images of a lamella prepared from an Fe film deposited on SLG and sulfurated at 300 °C. a) General overview of the complete pyrite layer (TEM-HAADF image) and b) same image colored by the overlapped EDX mapping. Orange rectangles delimit the compact (1) and porous (2) layers analyzed by EDX. The corresponding average atomic concentrations are shown in the tables at the bottom: left, compact layer; right, porous layer. c) and d) zoomed TEM-HAADF images of the compact and porous layers colored with the EDX mapping, respectively. Bottom right corner inserts correspond to the original TEM image.
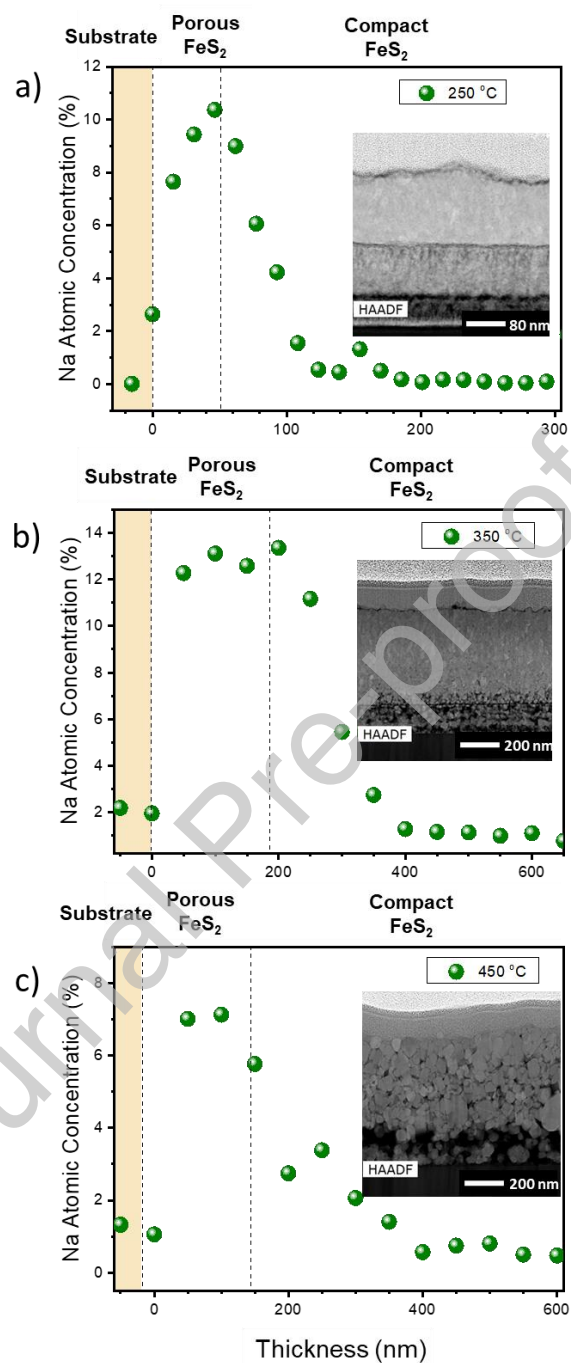
Figure 8

Figure 8. Sodium EDX line scan of pyrite films grown on SLG at a) 250 °C, b) 350 °C and c) 450 °C. Insert images correspond to the TEM-HAADF image of the complete pyrite films. Vertical dashed lines indicate the frontier between substrate, porous and compact layers, as indicated above.
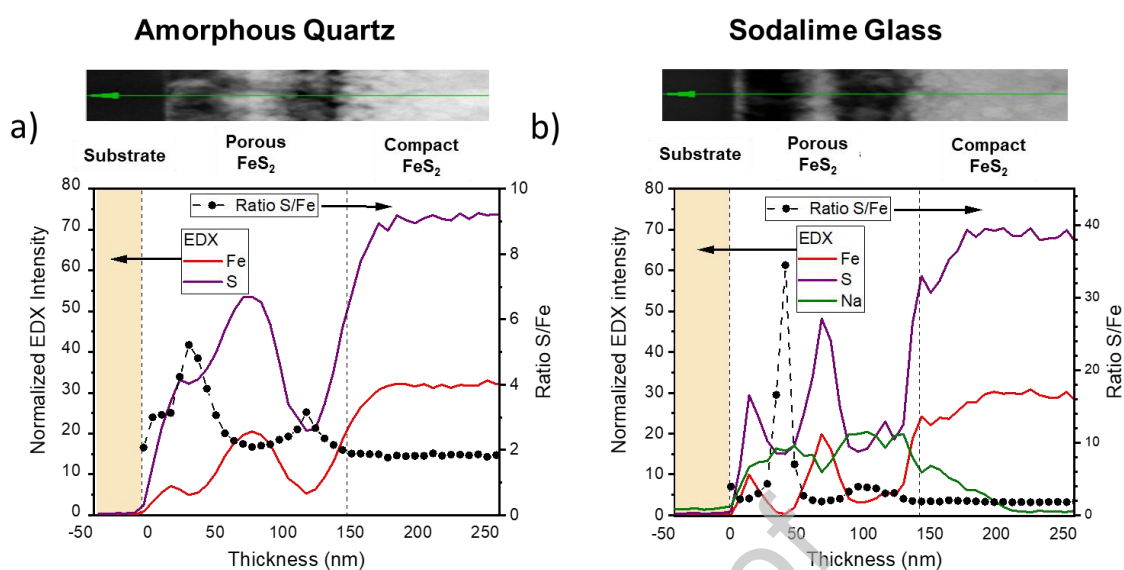
Figure 9

Figure 9. TEM-EDX line scan of pyrite films grown on a) quartz and b) SLG substrate sulfurated at $T_S = 350°C$. EDX signals from Na, Fe and S are shown as continuous lines (left axis), whereas a symbol-dashed line represents $S/_{Fe}$ ratio (right axis). As indicated, vertical dashed lines correspond to the frontier between substrate, porous and compact layers.
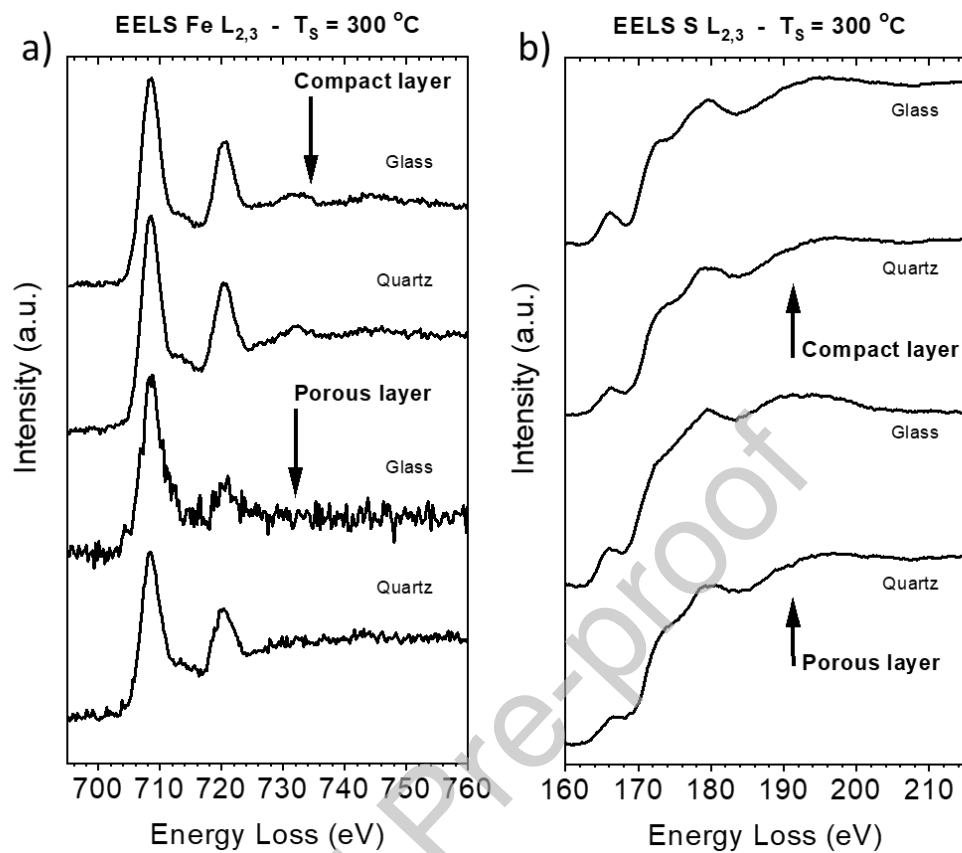
Figure 10

Figure 10. a) EELS Fe $L_{2,3}$ edge spectra of pyrite grains in the porous and compact layers of samples sulfurated at 300 °C on SLG and quartz substrates. b) The same for S $L_{2,3}$ edge.